



# A cluster-plus-glue-atom composition design approach designated for multi-principal element alloys

Xuan Liu, Hui-Bin Ke\*, Liang Wang, Yao-Jian Liang, Lin-Jing Wang, Ben-Peng Wang, Lu Wang, Qun-Bo Fan, Yun-Fei Xue

Received: 13 December 2021 / Revised: 3 March 2022 / Accepted: 11 March 2022 / Published online: 10 September 2022  
© Youke Publishing Co., Ltd. 2022

**Abstract** Multi-principal element alloys (MPEAs) have shown extraordinary properties in different fields. However, the composition design of MPEAs is still challenging due to the complicated interactions among principal elements (PEs), and even more challenging with precipitates formation. Precipitation can be either beneficial or detrimental in alloys, thus it is important to control precipitates formation on purpose during alloy design. In this work, cluster-plus-glue-atom model (CGM) composition design method which is usually used to describe short-range order in traditional alloys has been successfully extended to MPEAs for precipitation design. The key challenge of extending CGM to MPEAs is the determination of center atom since there are no solvent or solute in MPEAs. Research has found that the element type of center atom was related not only with chemical affinity, but also with atomic volume difference in MPEAs, which has inevitable effect on atomic arrangement. Based on experimental data of MPEAs with precipitates, it was found that elements with either stronger chemical affinity or larger volume difference with other PEs would occupy the center site of clusters. Therefore, a cluster index ( $P_C$ ), which considers both chemical affinity and atomic volume factors, was proposed to assist the determination of center atom in MPEAs. Based on the approach, a solid-solution Zr-Ti-V-Nb-Al BCC alloy was obtained by inhibiting the

precipitation, while precipitation-strengthened Al-Cr-Fe-Ni-V FCC alloy and Al-Co-Cr-Fe-Ni BCC alloy were designed by promoting the precipitation. Corresponding experimental results demonstrated that the approach could provide a relatively simple and accurate predication of precipitation and the compositions of precipitations were in line with PEs in cluster in MPEAs. The research may open an effective way for composition design of MPEAs with desired phase structure.

**Keywords** Multi-principal element alloy (MPEA); Composition design; Phase structure; Cluster-plus-glue-atom model (CGM)

## 1 Introduction

In recent years, multi-principal element alloys (MPEAs) have attracted much interest [1–5] due to their excellent performance [6–13]. Performance of alloys are closely related to their phase structures and vast efforts have been devoted to phase prediction in MPEAs [14–22].

At present, the most frequently used phase prediction methods for MPEAs are empirical criteria and CALPHAD (CALculation of PHase Diagram). Empirical criteria such as atomic size differences ( $\delta$ ) [14, 15], electronegativity difference ( $\Delta\chi$ ) [16], valance electron concentration (VEC) [17] and thermodynamic parameters ( $\Omega$ ) [18] are usually obtained by summarizing reported data, resulting in the limitation on alloy system. Similarly, CALPHAD relies on existing database, which mostly contain binary and limited ternary alloy systems, since the database for higher-order alloy systems is grossly imperfect yet [19–22]. Furthermore, empirical criteria and CALPHAD are useful in

X. Liu, H.-B. Ke\*, Y.-J. Liang, L.-J. Wang, B.-P. Wang,  
L. Wang, Q.-B. Fan, Y.-F. Xue  
School of Materials Science and Engineering, Beijing Institute of  
Technology, Beijing 100081, China  
e-mail: kehuibin@bit.edu.cn

L. Wang  
Institute of Advanced Structure Technology, Beijing Institute of  
Technology, Beijing 100081, China



macro-scale, but fall short in describing the short-range order (SRO) in alloys.

Cluster-plus-glue-atom model (CGM) method is based on the conception of SRO [23–25] and could be used to predict precipitations in solid solutions. In CGM method, atoms in solid solutions could be divided into cluster and glue atom ideally. Cluster is the coordination polyhedron composed of a center atom and its nearest neighbor atoms, while glue atoms are located in the interstitial sites [23]. In traditional alloys, solute atom is regarded as the center atoms, and other atoms could be located by comparing chemical affinity between solute and solvent elements [26, 27]. According to the theory, precipitations will form if the composition of center atom exceeds the value settled by CGM.

However, there is no clear distinction between solute and solvent in MPEAs, and the mutual interactions among multiple principal elements [28, 29] makes it difficult to determine the center atom element, which results in difficulties in applying CGM directly to MPEAs. Previous research demonstrated that the atomic arrangement in MPEAs is not only related to chemical affinity but also atomic volume [14, 15], as the volume differences between principal elements would result in severe lattice distortion, which is one of the key differences between MPEAs and traditional alloys. Thus, both chemical affinity and atomic volume difference should be considered when applying the CGM approach to MPEAs.

In this work, an improved CGM approach was proposed for MPEAs, the location of PEs was determined by an index considering both chemical and structural factors. Through this approach, a body-center-cubic-structure-based (BCC-based) light-weight solid-solution MPEA and two precipitation-strengthened MPEA were designed and confirmed by corresponding experiments. The results are expected to provide a composition design approach for MPEAs with the desired precipitation.

## 2 Experimental

### 2.1 General cluster-plus-glue-atom model

Previous study demonstrated that MPEAs are typically characterized as FCC and BCC structures [30–36]. According to the crystal structure of FCC, the FCC-CGM was built, as shown in Fig. 1a. Based on a  $2 \times 2 \times 2$  supercell, the basic cluster unit with periodical boundary was established. The formula could be written as follows:

$$C - N_{12} - (G_1^1 G_3^2 G_3^3 G_{12}^4) \quad (1)$$

where  $C$  is the center atom,  $N_n$  denotes there are  $n$  neighbor atoms in the cluster,  $G_n^x$  denotes there are  $n$  glue atoms at

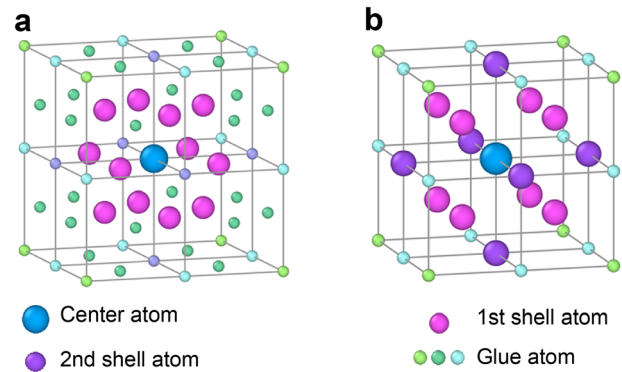


**Fig. 1** Atomistic packing model of basic CGM units in **a** FCC structure and **b** BCC structure

location  $x$  (1-vertex, 2-edge, 3-face center of original cell and 4-face center of supercell) of supercell. The cluster in FCC is a hexadecahoron consisted of one center atom and twelve neighbor atoms, and the coordination relation could be written as  $CN_{12}$ .

The CGM of BCC structure could be built in the same way (Fig. 1b) and it could be written as follows:

$$C - N_8^1 N_3^2 - G_1^1 G_3^2 \quad (2)$$

where  $N_n^1$  denotes that there are  $n$  first nearest neighbor atoms and  $N_n^2$  denotes that there are  $n$  second nearest neighbor atoms (the number of second nearest neighbor atom is three as  $N_n^2$  are located at the face center of the supercell). The cluster in BCC is a dodecahedron consisting of one center atom and fourteen neighbor atoms, and coordination relation could be written as  $CN_{14}$  since the second neighbor atoms occupied the face center site of basic cluster unit.

### 2.2 Material preparation

Master MPEA ingots were prepared by arc-melting pure metal with purity > 99.9% under a purified argon atmosphere. In order to improve chemical homogeneity, the ingots were re-melted at least four times. The ingots were then poured into a copper mold measuring 50 mm × 13 mm × 30 mm.

### 2.3 Material characterization

#### 2.3.1 Microstructure characterization

Phase structures of these MPEAs were characterized by synchrotron-based high-energy X-ray diffraction (HEXRD) technique. The tests were performed at the 11-ID-C beam line of the advanced photon source (APS) in Argonne National Laboratory. The wavelength used

here is  $\lambda = 0.011725$  nm, and the beam size was  $200 \mu\text{m} \times 200 \mu\text{m}$ .

Microstructure of MPEAs was investigated using spherical-aberration corrected transmission electron microscope (STEM, Hitachi S4800). The atomic resolution images were obtained by high-angle annular dark field (HAADF) detector. The samples were cut with diamond wire saw and then grinded with carborundum papers. After that, the samples were electro-polished with twin-jet electro-polishing and then corroded with Marble's reagent.

Precise composition analysis of MPEAs was performed by a CAMECA local electrode atom probe LEAPTM 4000X SI type three-dimensional atom probe tomography (APT). The experiment was carried out at a temperature of 20 K, under a pulsing laser with a pulse energy of 40 pJ, a pulse rate of 200 kHz, and an ion collection rate of 0.5% per pulse. A Zeiss Auriga focused-ion-beam (FIB)/SEM was used to fabricate a sharp tip specimen for APT analysis. Pt was deposited on the region of interest before FIB milling, and the wedge specimen was cut out and mounted on a pre-sharpened tip on a micro-post of a Si array coupon. At last, a sharp tip suitable for APT experiments (apex radius  $< 50$  nm) was produced by annular milling. Reconstruction and quantitative analysis of APT data were carried out by a CAMECA IVAS version 3.6.8 software.

### 2.3.2 Mechanical property characterization

Mechanical property of MPEAs was investigated by a universal electronic tensile testing machine (CMT4305). Flat, dog-bone-shaped tensile samples with a gauge size of  $10 \text{ mm} \times 3 \text{ mm} \times 1 \text{ mm}$  were cut by electrical discharge machining and then polished with carborundum paper to 2000-grit s. The tensile tests were carried out at room temperature ( $\sim 298$  K) at a strain rate of  $1 \times 10^{-3} \text{ s}^{-1}$ .

## 3 Results and discussion

### 3.1 Determination of cluster-glue atom model

#### 3.1.1 Theoretic model

For traditional alloys, the solute atoms were regarded as center atoms, and the position of other atoms in CGM were determined according to chemical enthalpy between solvent and solute. However, no clear distinction can be drawn between solvent and solute in MPEAs. Therefore, how to determine the center atom element is critical to applying CGM to MPEAs.

Resulting from the severe lattice distortion in MPEAs, the SRO cluster in MPEAs is not only related to chemical affinity but also atomic volume. According to that, three

factors were selected to characterize the atomic volume difference and chemical affinity between center atom and other principal elements:  $V_{\text{diff}}^i$  is the volume difference between  $i$ -th element and other PEs;  $\overline{\Delta H_{\text{chem}}^{i-\text{ave}}}$  and  $\Delta H_{\text{chem}}^{i-\text{SD}}$  are mean value and standard deviation of chemical enthalpy between  $i$ -th element and other PEs, respectively. The factors could be calculated as follows:

$$V_{\text{diff}}^i = \frac{V_i - \overline{V_{i-\text{other}}}}{\overline{V_{i-\text{other}}}} \quad (3)$$

$$\overline{V_{i-\text{other}}} = \frac{1}{n-1} \sum_{k=1, k \neq i}^n V_k \quad (4)$$

$$V_i = V_{mi} \times \rho_i / N_A \quad (5)$$

$$\Delta H_{\text{chem}}^{i-\text{ave}} = \frac{1}{n-1} \sum_{j=1, j \neq i}^n \Delta H_{\text{chem}}^{ij} \quad (6)$$

$$\Delta H_{\text{chem}}^{i-\text{SD}} = \sqrt{\frac{1}{n-1} \sum_{i=1, j \neq i}^n (\Delta H_{\text{chem}}^{ij} - \Delta H_{\text{chem}}^{i-\text{ave}})^2} \quad (7)$$

where  $V_{mi}$  is the molar volume of  $i$ -th element,  $N_A$  is Avogadro constant,  $\rho_i$  is the stacking density of  $i$ -th element,  $\Delta H_{\text{chem}}^{ij}$  is the chemical enthalpy between  $i$ -th element and  $j$ -th element in binary liquid alloys, which can be calculated from Miedema macroscopic model [27].

Objective to discuss chemical affinity and volume features of the center atoms in CGM, some reported MPEAs containing SRO were selected and summarized [37–44]. The calculation results are illustrated in Fig. 2. It can be obtained from the data that the center atoms have at least one of the following features: the  $\overline{\Delta H_{\text{chem}}^{\text{CA}-\text{ave}}}$  is more negative or the  $V_{\text{diff}}^{\text{CA}}$  is higher. The former means that the formation of SRO clusters is dominated by chemical enthalpy. As shown in Fig. 2a, in Ni-Fe-Co-Cr alloy [37], atomic volumes of principal elements are almost equivalent ( $|V_{\text{diff}}^i| < 0.02$ ) while Cr has a stronger chemical affinity to all other elements with  $\overline{\Delta H_{\text{chem}}^{\text{Cr}-\text{ave}}}$  being the lowest. It is the same with W in Mo-Nb-Ta-V-W [43, 44]. The later one means that the lattice distortion is the main driving force. For instance, when Pd was added into Ni-Fe-Co-Cr alloy (Fig. 2b), center atom site will be occupied by Pd as atomic volume difference between Pd and other elements is much larger ( $V_{\text{diff}}^{\text{Pd}} = 0.35$ ) [38]. The same is true for Zr/Hf in Ti-V-Zr-Nb-Mo-Hf-Ta-W [39], Ta in Mo-Nb-Ta-V-W [43, 44], as shown in Fig. 2c, f, respectively. And in some other MPEAs, both features would contribute to the center atoms. For example, Al would occupy the center atom site in Al-Co-Cr-Cu-Fe-Ni [41, 42], because of both the lower chemical enthalpy ( $\overline{\Delta H_{\text{chem}}^{\text{Al}-\text{ave}}} = -12.6 \text{ kJ}\cdot\text{mol}^{-1}$ ) and larger atomic volume ( $P_V^{\text{Al}} = 0.37$ ) (Fig. 2e); likewise, V in

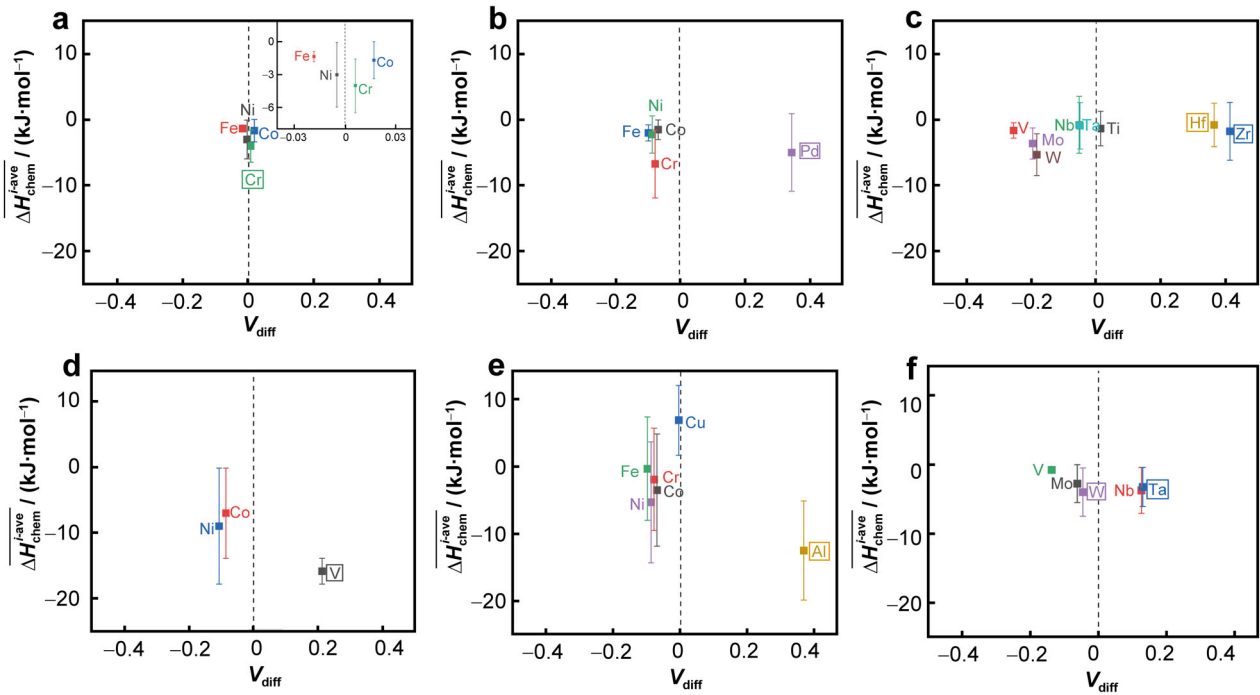


**Fig. 2** Volume difference between principal elements ( $V_{\text{diff}}^i$ ) and mean value of chemical enthalpy ( $\overline{\Delta H_{\text{chem}}^{i-\text{ave}}}$ ) with their standard deviation ( $\Delta H_{\text{chem}}^{i-\text{SD}}$ ), where elements in boxes are center atoms: **a** Ni-Fe-Co-Cr [37]; **b** Co-Cr-Fe-Ni-Pd [38]; **c** Ti-V-Zr-Nb-Mo-Hf-Ta-W [39]; **d** V-Co-Ni [40]; **e** Co-Cr-Cu-Fe-Ni-Al [41, 42]; **f** Mo-Nb-Ta-V-W [43, 44]

V-Co-Ni [40] (Fig. 2d). The center atoms here were obtained from the reported literature, and they were observed and determined through experimental results. For example, HADDF image indicated that introducing Pd promoted the formation of cluster in Co-Cr-Fe-Ni-Pd alloy and pair correlation functions revealed strong correlation peaks of Pd, Cr and Co [38]; TEM and APT revealed a nano-scaled  $L1_2$  phase in Al-Co-Cr-Fe-Ni-Cu, and it was originated from the selective occupation of Al in  $M_3Al$  phase (M means the mixture of Ni, Co, Cr) [41].

As stated above, the center atom of SRO cluster in MPEAs could be determined by considering both chemical affinity and atomic volume difference. In order to make the process of determining SRO cluster straightforward and calculatable, a cluster index ( $P_C$ ) considering both chemical affinity and atomic volume is proposed to determine the center atom element type, which is calculated as follows:

$$P_C^i = P_V^i + P_{\text{chem}}^i \quad (8)$$

where  $P_{\text{chem}}$  is the metric measuring the effect of chemical affinity;  $P_V$  is the metric measuring the effect of atomic volume factor; and  $P_{\text{chem}}$  and  $P_V$  are calculated as follows:

$$P_V^i = V_{\text{diff}}^i \quad (9)$$

$$P_{\text{chem}}^i = \Delta H_{\text{chem}}^{i-\text{ave}} / \Delta H_{\text{chem}}^{\text{ref}} \quad (10)$$

where  $V_{\text{diff}}^i$  and  $\Delta H_{\text{chem}}^{i-\text{ave}}$  are calculated based on Eqs. (3, 6), respectively,  $\Delta H_{\text{chem}}^{\text{ref}}$  is set to  $-10 \text{ kJ}\cdot\text{mol}^{-1}$  here, as it was reported as critical value of the formation of precipitation [18]. The stronger the chemical affinity between  $i$ -th element and other PEs is, the larger the  $P_{\text{chem}}^i$  is, meaning that there is a higher chance  $i$ -th element which would act as the center atom in CGM model; on the other hand, the larger the volume of  $i$ -th element than that of other elements is, the larger the  $P_V^i$  is, and there would be a higher chance  $i$ -th element which would act as the center atom in order to minimize lattice distortion caused by  $i$ -th element. When the chemical affinity between  $i$ -th element and other PEs is zero, then  $P_{\text{chem}}^i$  is equal to zero and only the atomic volume factor plays a role in determining the center atom; similarly, when the atomic volume of  $i$ -th element is equal to the average atomic volume of other PEs, then  $P_V^i$  equals to zero, and only the chemical affinity factor determines the center atom element type. Besides, glue atoms could be the PEs with low  $P_C$ . Figure 3 gives cluster index in the material systems shown in Fig. 2. As can be seen, for all the systems studied, PEs with the highest  $P_C$  were observed as the center atoms; PEs with low  $P_C$  tend to be glue atoms, such as Co, Fe and Ni in Al-Co-Cr-F-Ni-Ti alloy; and PEs with  $P_C$  in between would occupy the neighbor atom sites, such as Ni in Al-Co-Cr-Fe-Ni-Ti alloy.

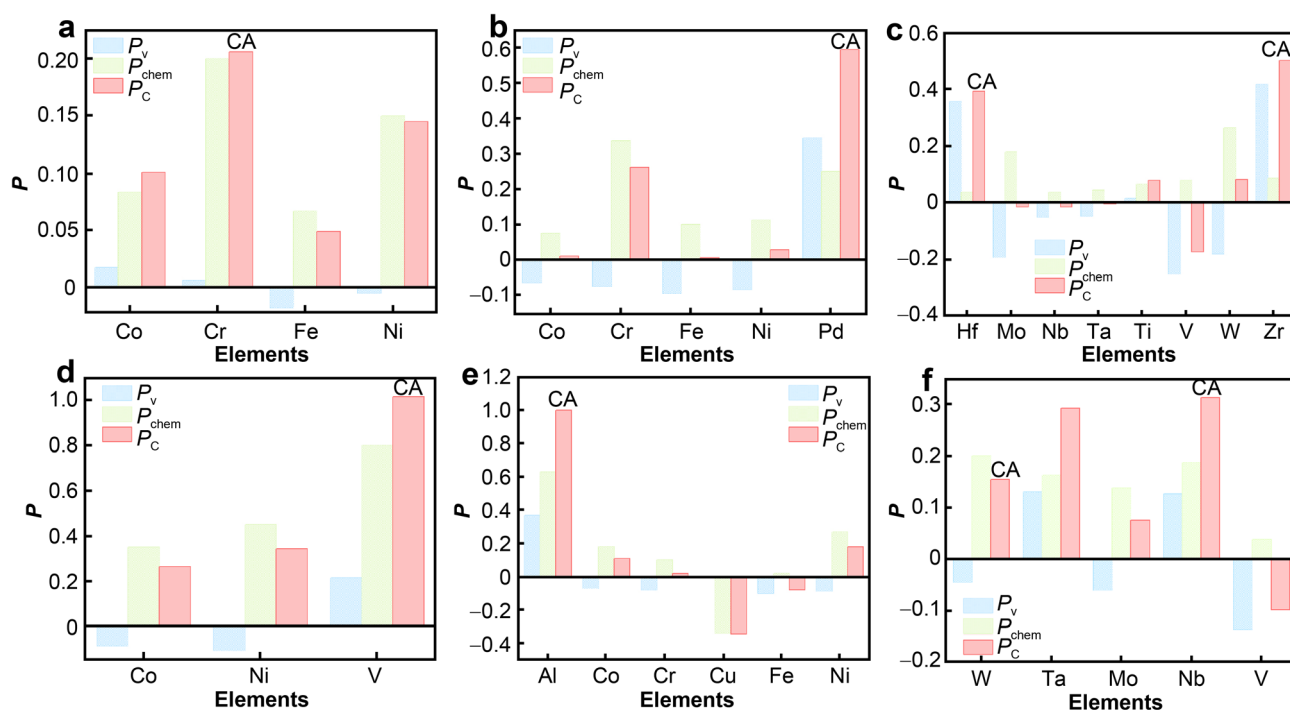


**Fig. 3** Cluster index of principal elements in selected MPEAs: **a** Ni-Fe-Co-Cr [37]; **b** Co-Cr-Fe-Ni-Pd [38]; **c** Ti-V-Zr-Nb-Mo-Hf-Ta-W [39]; **d** V-Co-Ni [40]; **e** Co-Cr-Cu-Fe-Ni-Al [41, 42]; **f** Mo-Nb-Ta-V-W [43, 44]

### 3.2 Validation

In order to validate the feasibility and correctness of the approach, two types of MPEA alloys, one with single solid-solution phase and the other with second strengthening phase in solid-solution matrix, were selected to conduct composition design with CGM followed by experimental validation. For single solid-solution (SS) alloy, Zr-Ti-V-Nb-Al alloy was selected to obtain light-weight alloy with single solid-solution structure; for precipitation-strengthened (PS) alloy, compositions of Al-Cr-Fe-Ni-V FCC alloy and Al-Co-Cr-Fe-Ni BCC alloy were optimized to obtain precipitation-strengthened alloy.

#### 3.2.1 Single solid solution Zr-Ti-V-Nb-Al alloy

Previous research demonstrated that the complex precipitates in current light-weight MPEAs limited the mechanical properties [45–49]. In the present work, Zr-Ti-V-Nb-Al system with mainly BCC phase was selected, and purpose

is to obtain a single BCC solid-solution light-weight alloy by avoiding precipitation.

CGMs of Zr-Ti-V-Nb-Al alloy was built based on the BCC-based general model as demonstrated in Sect. 2.1. To determine the position of PEs in BCC CGM,  $P_c$  of PEs was calculated, as shown in Fig. 4a. It could be seen that the  $P_c$  of Zr and Al is much higher than that of the other PEs and therefore should be regarded as cluster atoms. Considering that chemical affinity between Al and other PEs is much stronger ( $P_{chem}^{Al} = 1.35$ ,  $\Delta H_{chem}^{Al-i} < -15 \text{ kJ}\cdot\text{mol}^{-1}$ ) while chemical enthalpy between other PEs is very close to zero, and the four PEs besides Al are adjacent to each other in the periodic table, Al should be regarded as center atom and Zr could be determined as neighbor atoms in cluster. When it comes to Ti, V and Nb, Nb and V were chosen to occupy glue atom site as their  $P_c$  is the lowest and chemical enthalpy between them and cluster atoms is relatively weaker; Ti was also placed in neighbor atom set here as  $P_c^{Ti}$  is relatively high and the chemical affinity between Ti and center atom is very strong



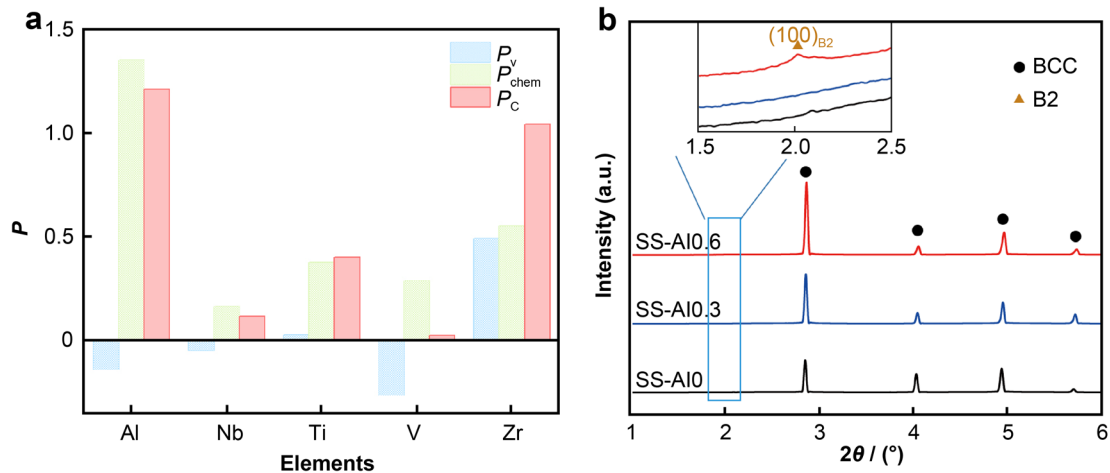


**Fig. 4** a Cluster index of principal elements in Zr-Ti-V-Nb-Al alloy; b HEXRD patterns of SS-Al<sub>x</sub> alloys

**Table 1** Chemical enthalpy ( $\Delta H_{\text{chem}}$ ) between PEs in Zr-Ti-V-Nb-Al alloy ( $\text{kJ}\cdot\text{mol}^{-1}$ ) [27]

PEs	Al	Ti	V	Zr	Nb
Al	0	-30	-16	-44	-18
Ti		0	-2	0	2
V			0	-4	-1
Zr				0	4
Nb					0

( $\Delta H_{\text{chem}}^{\text{Al-Ti}} = -30 \text{ kJ}\cdot\text{mol}^{-1}$ ), as can be seen in Table 1. What's more, the high content of Ti is beneficial to reduce the density of alloy, as the density of Ti is lower ( $\rho_{\text{Ti}} = 4.51 \text{ g}\cdot\text{cm}^{-3} < \rho_{\text{V}} = 6.00 \text{ g}\cdot\text{cm}^{-3} < \rho_{\text{Zr}} = 6.52 \text{ g}\cdot\text{cm}^{-3} < \rho_{\text{Nb}} = 8.57 \text{ g}\cdot\text{cm}^{-3}$ ). Based on the above, the CGM of Zr-Ti-V-Nb-Al alloy was preliminarily determined as  $[\text{Al}_1 - (\text{TiZr})_{11}] - (\text{VNb})_4$ , and the increase in center atom Al ( $> 6.25 \text{ at}\%$ ) would promote the precipitation process.

In order to validate the composition design, Al<sub>x</sub>-Ti<sub>2</sub>Zr<sub>1.2</sub>V<sub>0.8</sub>Nb alloys (SS-Al<sub>x</sub>,  $x = 0, 0.3, 0.6$ , and the composition of Al is 0%, 5.7% and 10.7%, respectively) were selected since the compositions were similar to Al<sub>0.33</sub>Ti<sub>2</sub>ZrVNb composition whose center atom Al changed. The SS-Al<sub>x</sub> alloys were prepared and characterized [50]. HEXRD patterns demonstrated that the main phase in SS-Al<sub>x</sub> alloys was BCC solid-solution phase (Fig. 4b). However, by enlarging HEXRD curves from  $1.5^\circ$  to  $2.5^\circ$ , a peak around  $2^\circ$  was found in the curve of SS-Al0.6 and the peak was identified as (100) peak of B2 phases. That is to say, with the increase in Al content, SS-Al<sub>x</sub> alloys transformed from BCC solid-solution phase to ordered B2 phase. Composition analysis confirmed that cluster atoms (Zr, Al) are enriched in ordered B2 [50]. The result is consistent with the composition design.

To reveal Al effect on the mechanical properties, the tensile true stress-strain curves of SS-Al<sub>x</sub> alloys were characterized and the addition of Al would significantly improve the yield strength without ductility reduction when there is no B2 precipitation; once the B2 phase is induced (SS-Al0.6), the ductility reduced rapidly [50]. Taking density into consideration, the specific yield strengths of SS-Al0.3 is up to  $166.05 \text{ MPa}\cdot\text{m}^3\cdot\text{kg}^{-1}$  (Table 2), higher than most of the reported MPEAs with tensile ductility [50].

### 3.2.2 Precipitation-strengthened alloy

At the primary stage of MPEAs, single-phase solid solution alloys were managed to be fabricated because intermetallic precipitates were regarded as detrimental phase as they may degenerate the properties of MPEAs [3, 11–13, 51]. However, some studies indicated that the secondary phases in MPEAs could also contribute significantly to improve the mechanical properties [52–60], like those in most engineering alloys.

**3.2.2.1 FCC-based Al-Cr-Fe-Ni-V alloy** Al-Cr-Fe-Ni based alloy is a well-studied MPEAs, and previous study demonstrated that the Ni<sub>3</sub>Al-type L<sub>12</sub>-structured precipitation in FCC-based alloy is beneficial to the improvement of alloy strength [12], and V plays an important role in the

**Table 2** Density and specific yield strength of SS-Al<sub>x</sub>

Alloy	Density / ( $\text{g}\cdot\text{cm}^{-3}$ )	Specific yield strength / ( $\text{MPa}\cdot\text{m}^3\cdot\text{kg}^{-1}$ )
SS-Al0	5.964	156.27
SS-Al0.3	5.920	166.05
SS-Al0.6	5.813	83.95

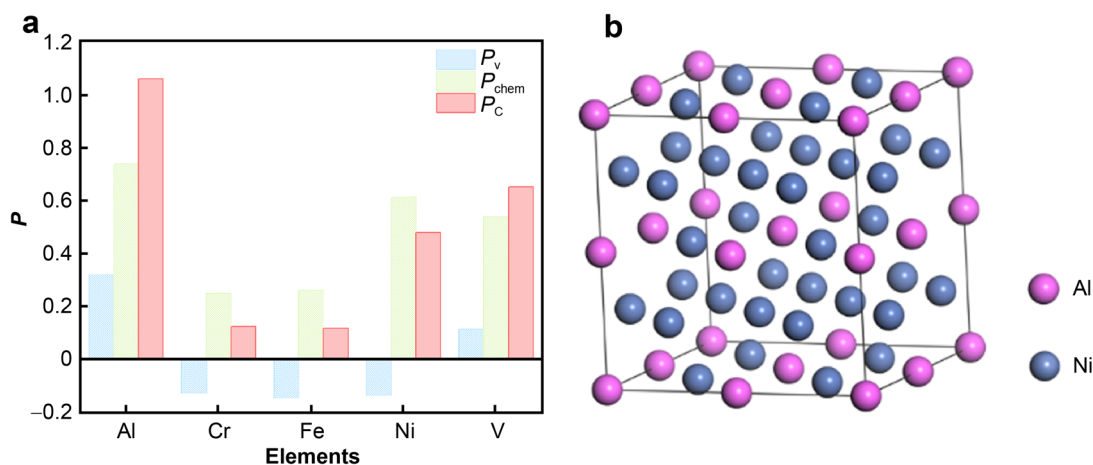


**Fig. 5** a Cluster index of principal elements in Al-Cr-Fe-Ni-V alloy; b cluster-glue-atom model of  $\text{Ni}_3$

**Table 3**  $\Delta H_{\text{chem}}$  between PEs in Al-Cr-Fe-Ni-V alloy ( $\text{kJ}\cdot\text{mol}^{-1}$ ) [27]

PEs	Al	Cr	Fe	Ni	V
Al	0	-10	-11	-22	-16
Cr		0	-1	-7	-2
Fe			0	-2	-7
Ni				0	-18
V					0

precipitation process in Cr-Fe-Ni-V alloy according to the research by Choi et al. [61]. Therefore, Al-Cr-Fe-Ni-V alloy was selected to obtain precipitation-strengthened MPEAs by controlling the formation and structure of precipitates.

To determine the threshold composition to form precipitates in Al-Cr-Fe-Ni-V alloy, CGM was built based on the FCC-based general model demonstrated in Sect. 2.1. To determine the center atom element of CGM, cluster index of principal elements in Al-Cr-Fe-Ni-V alloy were calculated, as illustrated in Fig. 5a, and chemical enthalpy between PEs is listed in Table 3. It could be seen that the  $P_C$  of Al is the largest, while those of Cr and Fe are significantly smaller ( $P_C^{\text{Fe}} = 0.12$ ,  $P_C^{\text{Cr}} = 0.13$ ). Therefore, Al would occupy the center atom position from structural aspect, Cr and Fe would occupy the glue atom position. For the other two principal elements V and Ni, their  $P_C$  were in the middle, and chemical affinity between center atom and the two elements were regarded as the priority consideration. Compared to V, chemical affinity between Ni and center atom Al is stronger ( $\Delta H_{\text{chem}}^{\text{Al-Ni}} = -22 \text{ kJ}\cdot\text{mol}^{-1}$ ,  $\Delta H_{\text{chem}}^{\text{V-Ni}} = -16 \text{ kJ}\cdot\text{mol}^{-1}$ ); and chemical affinity between V and Ni is also stronger than that between V and Al. Thus, Ni would occupy the neighbor atom site and V would occupy the center atom site in the cluster-glue-atom

formula. According to this, the CGF of Al-Cr-Fe-Ni-V alloy could be written as  $[(\text{AlV}) - \text{Ni}_{12}] - (\text{CrFeAlVNi})_{19}$ .

To obtain desired  $\text{Ni}_3\text{Al}$ -type  $\text{L}_{12}$ -structured precipitates, the CGM could be modified by referring to cluster formula of  $\text{Ni}_3\text{Al}$  (Fig. 5b). According to the cluster-glue-atom model of  $\text{Ni}_3\text{Al}$ , the glue atoms are  $\text{Al}_7\text{Ni}_{12}$ , and the glue atom in Al-Cr-Fe-Ni-V alloy could be written as  $[(\text{AlV})\text{CrFe}]_7 - (\text{NiCrFe})_{12}$ . The contribution of Fe and Cr could be considered to be the same and occupied the sites randomly, as  $\Delta H_{\text{chem}}^{\text{Fe-Cr}}$  is  $-1 \text{ kJ}\cdot\text{mol}^{-1}$  and the atomic volumes of Fe and Cr are very similar (the molar volume of Cr is  $7.23 \times 10^{-6} \text{ m}^3\cdot\text{mol}^{-1}$  and that of Fe is  $7.10 \times 10^{-6} \text{ m}^3\cdot\text{mol}^{-1}$ ). Accordingly, the CGM of FCC-based Al-Cr-Fe-Ni-V alloy could be written as  $[(\text{AlV}) - \text{Ni}_{12}] - [(\text{AlV})_{7/3}\text{Cr}_{7/3}\text{Fe}_{7/3}](\text{Ni}_4\text{Cr}_4\text{Fe}_4)$ , and the corresponding composition is  $(\text{AlV})_{0.52}\text{CrFeNi}_{2.52}$ .

To validate the designed compositions, two Al-Cr-Fe-Ni-V alloy,  $\text{Al}_{0.5}\text{CrFeNi}_{2.5}$  (PS-V0) alloy and  $\text{Al}_{0.5}\text{CrFeNi}_{2.5}\text{V}_{0.2}$  (PS-V0.2) alloy whose compositions were similar to  $(\text{AlV})_{0.52}\text{CrFeNi}_{2.52}$ , the composition changes of center atom V were analyzed. The PS alloys were prepared and phase structures were analyzed by means of synchrotron HEXRD [62]. It could be seen that PS alloys mainly consist of FCC-structured matrix and  $\text{L}_{12}$ -structured precipitation (Fig. 6a). HEXRD patterns of PS-0.2 alloy exhibited a higher peak of  $\text{L}_{12}$  phase, proving that the addition of center atom V could promote the formation of precipitation. What's more, the quantitative analysis results revealed that the  $\text{L}_{12}$ -structured precipitations were major precipitations ( $\sim 50\%$ ) in the PS-V0.2 alloy whereas the fraction of the BCC-structured precipitations was barely  $\sim 6\%$  [62].

To obtain elemental distribution in FCC matrix and  $\text{L}_{12}$  precipitation, one-dimensional concentration profiles of PS-0.2 alloy are shown in Fig. 6b, and mean compositions

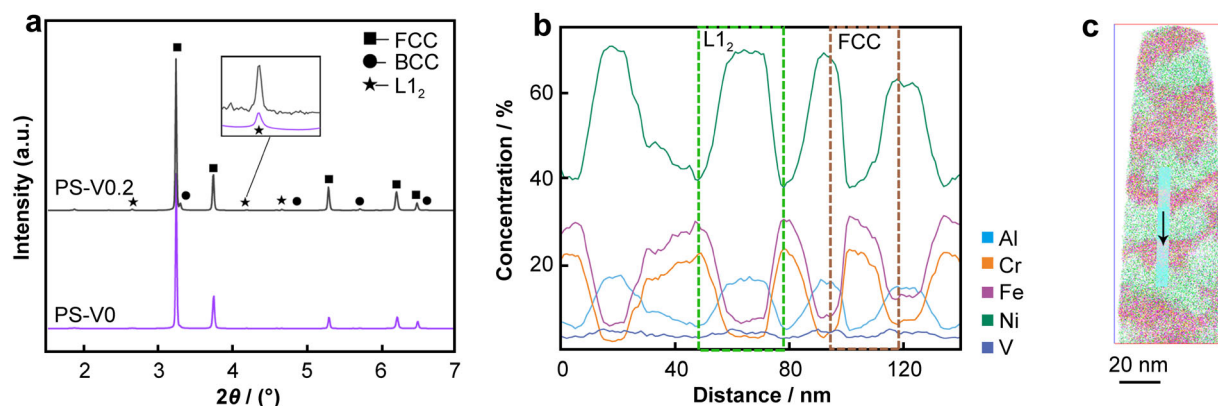


**Fig. 6** Phase structure and element distribution in PS alloys: **a** HEXRD patterns PS alloys; **b** 1D concentration profile of PS-V0.2 alloy detected by 3DAP; **c** sampling position displayed in reconstruction of PS-V0.2 alloy

**Table 4** Mean compositions of FCC matrix and  $L_{12}$  precipitations (at%)

Phase	Al	Cr	Fe	Ni	V
FCC matrix	5.08	25.01	29.56	37.51	2.84
$L_{12}$ precipitation	18.17	2.53	6.49	68.04	4.77

of the two phases were calculated, as listed in Table 4. It could be found that cluster atoms with larger  $P_C$  (Al, V and Ni) enrich in the  $L_{12}$  precipitation and glue atoms with smaller  $P_C$  (Cr and Fe) enrich in FCC matrix, confirming that the elemental distribution after phase separation could be predicted by comparing  $P_C$  of principal elements.

To prove strengthening effect of  $L_{12}$  precipitation, the tensile engineering stress–strain curves were measured and showed remarkable increases in strength ( $> 1.5$  GPa). The PS-V0.2 alloy exhibited ultrahigh yield strength of 1,821 MPa and good strain-hardening capacity with useful ductility ( $\sim 5\%$ ) [62]. The increase in strength confirmed that precipitation-strengthened MPEA could be obtained by the improved CGM approach.

**3.2.2.2 BCC-based alloy** Previous studies have shown that B2 phase in FCC-based alloy is unfavorable to the plasticity due to its semi coherent relationship with the matrix; however, B2 phase is the preferred strengthening phase of BCC system alloy [63]. Based on the research of Al-Co-Cr-Fe-Ni alloy, composition design research was carried out to obtain NiAl type B2 ordered phase in BCC solid solution matrix.

CGM of Al-Co-Cr-Fe-Ni alloy was built based on the BCC-based general model demonstrated in Sect. 2.1.

Cluster indexes of principal elements in Al-Co-Cr-Fe-Ni alloy are plotted in Fig. 7a, and chemical enthalpies between PEs are listed in Table 5. Similar to Al-Cr-Fe-Ni-V alloy, Al and Ni would occupy the center atom position and nearest neighbor atom position, respectively. Similar to Fe and Cr, Co would occupy the glue atom position. Besides, to obtain NiAl type B2 ordered phase, the atomic ratio of Al and Ni was controlled ( $c_{Al}/c_{Ni} \approx 1/1$ ). Therefore, CGM of Al-Co-Cr-Fe-Ni alloy could be written as  $[Al_1 - Ni_1(FeCoCr)_7(FeCoCr)_3] - (FeCoCr)_4$ , and corresponding composition is  $Al_{0.25}Ni_{0.25}(CoCrFe)_{3.5}$ . For Al-Co-Cr-Fe-Ni alloy, the formation of B2 phase would be promoted when the content of Al and Ni increases as the leading factor is strong chemical affinity of Al-Ni.

The composition of  $Al_{0.3}Co_{0.7}Cr_{1.3}FeNi_{0.3}$  (PS-BN) alloy is similar to the designed composition, and the contents of Al and Ni (8.33 at%) are slightly higher than the critical value (6.25 at%). Therefore, it is expected that a certain amount of B2 phase would form in the BCC-structured matrix. Characterized phase structure of PS-BN alloy is shown in Fig. 7b–d. HEXRD pattern in Fig. 7b proved that main phase of the alloy is BCC-structured solid-solution, and the diffraction peak in  $2\theta = 2.4^\circ$  indicated the existence of B2 phase. STEM image and selected area electron diffraction (SAED) pattern (Fig. 7c) further revealed that the spherical nanoparticles in the alloy were B2 phase and the fraction of precipitated phase was high ( $\sim 50\%$ ). In addition, energy dispersive X-Ray spectroscopy (EDX) scanning (Fig. 7d) indicated that Al and Ni were enriched in B2 phase, and Cr and Fe were enriched in BCC matrix, which is consistent with the calculated  $P_C$ . This result further verified the applicability of CGM to design PS-MPEAs.



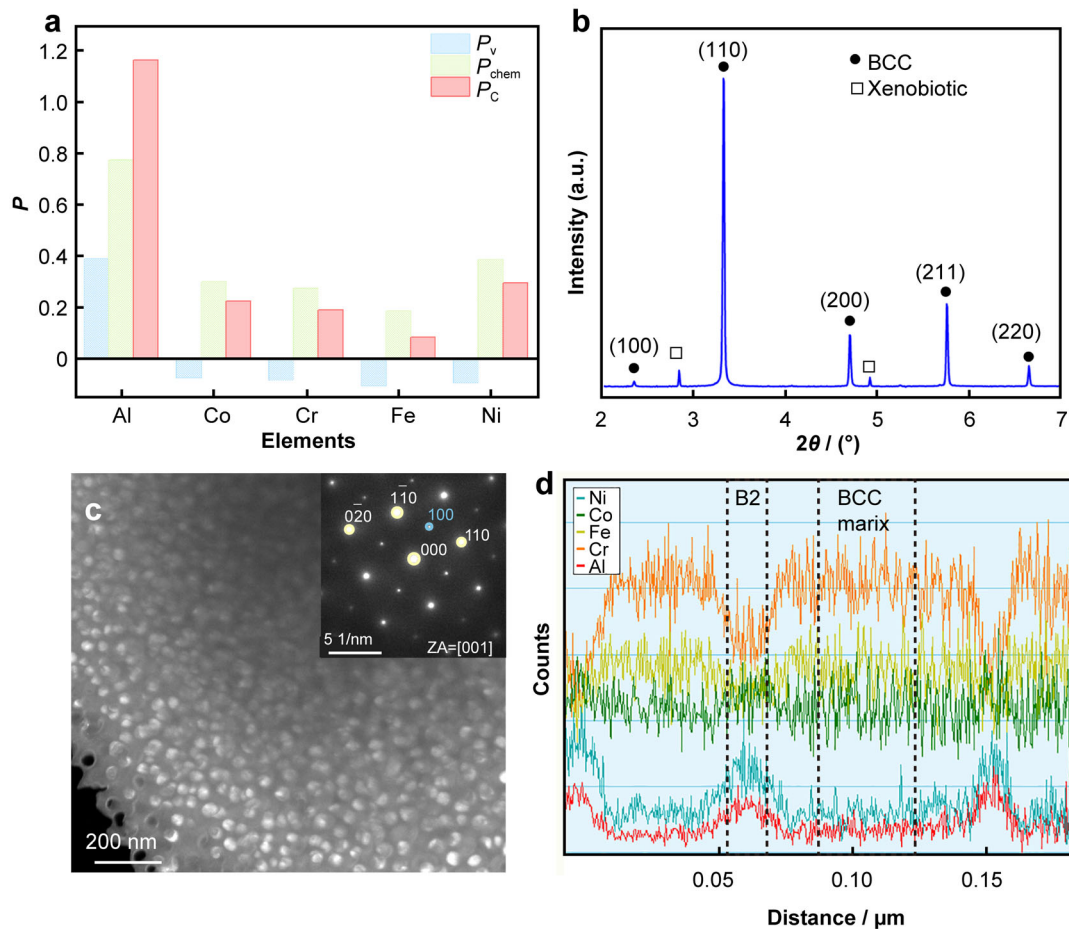


**Fig. 7** a Cluster index of principal elements in Al-Co-Cr-Fe-Ni alloy. Phase structure of PS-BN alloy: b HEXRD pattern; c HAADF-STEM image and (inset) SAED patterns; d one-dimensional EDX scanning curve of two phases

**Table 5**  $\Delta H_{chem}$  between PEs in Al-Co-Cr-Fe-Ni (kJ·mol<sup>-1</sup>) [27]

PEs	Al	Cr	Co	Fe	Ni
Al	0	-10	-19	-11	-22
Cr		0	-4	-1	-7
Co			0	-1	0
Fe				0	-2
Ni					0

## 4 Conclusion

To design precipitation in MPEAs, a cluster index ( $P_c$ ) considering both chemical affinity and lattice distortion has been proposed to determine the center atom element in CGM, which is the key question when extending CGM to MPEAs. It is found and confirmed by experimental results that  $P_c$  can be used to quickly determine cluster atom and glue atom in MPEAs, therefore control formation of precipitates in MPEAs. Based on the approach, a BCC-based

light-weight solid-solution Zr-Ti-V-Nb-Al MPEAs (SS-MPEAs) and two precipitation-strengthened MPEAs (PS-MPEAs) were studied, and both alloys were confirmed by experiments with desired phase structures according to calculation results. The phase structure of SS alloys transfers from single BCC phase to BCC + B2 phase, as the composition of Al increases; the PS-FN alloys were consisted of FCC-structured matrix and  $L1_2$ -structured precipitation, the PS-BN alloy was consisted of BCC-structured matrix and B2-structured precipitation.

**Acknowledgements** This study was financially supported by the China Postdoctoral Science Foundation (No. 2019M660482). Use of the Advanced Photon Source is supported by the U. S. Department of Energy, Office of Science, Office of Basic Energy Sciences, under Contract No. DE-AC02-06CH11357. We thank Dr. S.B. Jin and Dr. G. Sha at the Materials Characterization Facility of Nanjing University of Science for APT characterization.

## Declarations

**Conflict of interests** The authors declare that they have no conflict of interest.

## References

- [1] Zhang W, Liaw PK, Zhang Y. Science and technology in high-entropy alloys. *Sci China Mater.* 2018;61(1):2. <https://doi.org/10.1007/s40843-017-9195-8>.
- [2] Cantor B, Chang ITH, Knight P, Vincent AJB. Microstructural development in equiatomic multicomponent alloys. *Mater Sci Eng.* 2004;375:213. <https://doi.org/10.1016/j.msea.2003.10.25>.
- [3] Yeh JW, Chen SK, Lin SJ, Gan JY, Chin TS, Shun TT, Tsau CH, Chang SY. Nanostructured high-entropy alloys with multiple principal elements: novel alloy design concepts and outcomes. *Adv Eng Mater.* 2004;6(5):299. <https://doi.org/10.1002/adem.200300567>.
- [4] Lu ZP, Wang H, Chen MW, Baker I, Yeh JW, Liu CT, Nieh TG. An assessment on the future development of high-entropy alloys: summary from a recent workshop. *Intermetallics.* 2015; 66:67. <https://doi.org/10.1016/j.intermet.2015.06.021>.
- [5] Pickering EJ, Jones NG. High-entropy alloys: a critical assessment of their founding principles and future prospects. *Int Mater Rev.* 2016;61(3):183. <https://doi.org/10.1080/09506608.2016.1180020>.
- [6] Chuang MH, Tsai MH, Wang WR, Lin SJ, Yeh JW. Microstructure and wear behavior of  $Al_xCo_{1.5}CrFeNi_{1.5}Ti_y$  high-entropy alloys. *Acta Mater.* 2011;59(16):6308. <https://doi.org/10.1016/j.actamat.2011.06.041>.
- [7] Zou Y, Ma H, Spolenak R. Ultrastrong ductile and stable high-entropy alloys at small scales. *Nat Commun.* 2015;6: 7748. <https://doi.org/10.1038/ncomms8748>.
- [8] Wu YD, Cai YH, Wang T, Si JJ, Zhu J, Wang YD, Hui XD. A refractory  $Hf_{25}Nb_{25}Ti_{25}Zr_{25}$  high-entropy alloy with excellent structural stability and tensile properties. *Mater Lett.* 2014;130: 277. <https://doi.org/10.1016/j.matlet.2014.05.134>.
- [9] Deng Y, Tasan CC, Pradeep KG, Springer H, Kostka A, Raabe D. Design of a twinning-induced plasticity high entropy alloy. *Acta Mater.* 2015;94:124. <https://doi.org/10.1016/j.actamat.2015.04.014>.
- [10] Li D, Li C, Feng T, Zhang Y, Sha G, Lewandowski JJ, Liaw PK, Zhang Y. High-entropy  $Al_{0.3}CoCrFeNi$  alloy fibers with high tensile strength and ductility at ambient and cryogenic temperatures. *Acta Mater.* 2017;123:285. <https://doi.org/10.1016/j.actamat.2016.10.038>.
- [11] Gludovatz B, Hohenwarter A, Catoor D, Chang EH, George EP, Ritchie RO. A fracture-resistant high-entropy alloy for cryogenic applications. *Sci China Mater.* 2014;345(6201):1153. <https://doi.org/10.1016/j.actamat.2016.10.038>.
- [12] Tang Z, Yuan Y, Tsai CW, Yeh JW, Lundin CD, Liaw PK. Fatigue behavior of a wrought  $Al_{0.5}CoCrCuFeNi$  two-phase high-entropy alloy. *Acta Mater.* 2015;99:247. <https://doi.org/10.1016/j.actamat.2015.07.004>.
- [13] Hemphill MA, Yuan T, Wang GY, Yeh JW, Tsai CW, Chuang A, Liaw PK. Fatigue behavior of  $Al_{0.5}CoCrCuFeNi$  high entropy alloys. *Acta Mater.* 2012;60(16):5723. <https://doi.org/10.1016/j.actamat.2012.06.046>.
- [14] Zhang Y, Zhou YJ, Lin JP, Chen GL, Liaw PK. Solid-solution phase formation rules for multi-component alloys. *Adv Eng Mater.* 2008;10(6):534. <https://doi.org/10.1002/adem.200700240>.
- [15] Wang Z, Huang Y, Yang YY, Wang Y, Liu CT. Atomic-size effect and solid solubility of multicomponent alloys. *Scripta Mater.* 2015;94:28. <https://doi.org/10.1016/j.scriptamat.2014.09.010>.
- [16] Poletti MG, Battezzati L. Electronic and thermodynamic criteria for the occurrence of high entropy alloys in metallic systems. *Acta Mater.* 2014;75:297. <https://doi.org/10.1016/j.actamat.2014.04.033>.
- [17] Guo S, Ng C, Lu J, Liu CT. Effect of valence electron concentration on stability of fcc or bcc phase in high entropy alloys. *J Appl Phys.* 2011;109(10): 103505. <https://doi.org/10.1063/1.3587228>.
- [18] King DJM, Middleburgh SC, McGregor AG, Cortie MB. Predicting the formation and stability of single phase high-entropy alloys. *Acta Mater.* 2016;104:172. <https://doi.org/10.1016/j.actamat.2015.11.040>.
- [19] Zhang C, Zhang F, Chen S, Cao W. Computational thermodynamics aided high-entropy alloy design. *JOM.* 2012;64(7):839. <https://doi.org/10.1007/s11837-012-0365-6>.
- [20] Zhang F, Zhang C, Chen SL, Zhu J, Cao WS, Kattner UR. An understanding of high entropy alloys from phase diagram calculations. *Calphad.* 2014;45:1. <https://doi.org/10.1016/j.calphad.2013.10.006>.
- [21] Morral JE, Chen S. A regular solution model for a single-phase high entropy and enthalpy alloy. *J Phase Equilib Diffus.* 2017; 38(4):382. <https://doi.org/10.1007/s11669-017-0578-z>.
- [22] He F, Wang Z, Wu Q, Niu S, Li J, Wang J, Liu CT. Solid solution island of the Co-Cr-Fe-Ni high entropy alloy system. *Scripta Mater.* 2017;131:42. <https://doi.org/10.1016/j.scriptamat.2016.12.033>.
- [23] Dong C, Wang Q, Qiang JB, Wang Y, Jiang N, Han G, Li Y, Wu J. Topical review: from clusters to phase diagrams: composition rules of quasicrystals and bulk metallic glasses. *J Phys D Appl Phys.* 2007;40(15):273. <https://doi.org/10.1088/0022-3727/40/15/R01>.
- [24] Hong HL, Wang Q, Dong C, Liaw PK. Understanding the Cu-Zn brass alloys using a short-range-order cluster model: significance of specific compositions of industrial alloys. *Sci Rep.* 2014;4(2): 7065. <https://doi.org/10.1038/srep07065>.
- [25] Pang C, Jiang B, Shi Y, Wang Q, Dong C. Cluster-plus-gluon-atom model and universal composition formulas [cluster](glue atom)<sub>x</sub> for BCC solid solution alloys. *J Alloy Compd.* 2015;652:63. <https://doi.org/10.1016/j.jallcom.2015.08.209>.
- [26] Takeuchi A, Inoue A. Classification of bulk metallic glasses by atomic size difference, heat of mixing and period of constituent elements and its application to characterization of the main alloying element. *Mater Trans.* 2005;46(12):2817. <https://doi.org/10.2320/matertrans.46.2817>.
- [27] Takeuchi A, Inoue A. Calculations of mixing enthalpy and mismatch entropy for ternary amorphous alloys. *Mater Trans, JIM.* 2007;41(11):1372. <https://doi.org/10.2320/matertrans1989.41.1372>.
- [28] Yeh JW. Recent progress in high-entropy alloys. *Annales de Chimie Science des Matériaux.* 2006;31(6):633. <https://doi.org/10.3166/acsm.31.633-648>.
- [29] Ranganathan S. Alloyed pleasures: multimetallic cocktails. *Curr Sci.* 2003;85(5):3. <https://doi.org/10.1038/nature02146>.
- [30] Lu YP, Dong Y, Guo S, Jiang J, Kang HJ, Wang YM, Wen B, Wang ZJ, Jie JC, Cao ZQ, Ruan HH, Li TJ. A promising new class of high-temperature alloys: eutectic high-entropy alloys. *Sci Rep.* 2014;4:6200. <https://doi.org/10.1038/srep06200>.
- [31] Wani IS, Bhattacharjee T, Sheikh S, Lu YP, Chatterjee S, Bhattacharjee PP, Guo S, Tsuji N. Ultrafine-grained AlCoCrFeNi<sub>21</sub> eutectic high-entropy alloy. *Mater Res Lett.* 2016;4(3): 174. <https://doi.org/10.1080/21663831.2016.1160451>.
- [32] Kao YF, Chen TJ, Chen SK, Yeh JW. Microstructure and mechanical property of as-cast, homogenized, and deformed  $Al_xCoCrFeNi$  ( $0 \leq x \leq 2$ ) high-entropy alloys. *J Alloy Compd.* 2009;488(1):57. <https://doi.org/10.1016/j.jallcom.2009.08.090>.
- [33] Li C, Li JC, Zhao M, Jiang Q. Effect of aluminum contents on microstructure and properties of  $Al_xCoCrFeNi$  alloys. *J Alloy Compd.* 2010;504:515. <https://doi.org/10.1016/j.jallcom.2010.03.111>.

- [34] Wang WR, Wang WL, Wang SC, Tsai YC, Lai CH, Yeh JW. Effects of Al addition on the microstructure and mechanical property of  $\text{Al}_x\text{CoCrFeNi}$  high-entropy alloys. *Intermetallics*. 2012;26:44. <https://doi.org/10.1016/j.intermet.2012.03.005>.
- [35] Wang WR, Wang WL, Yeh JW. Phases, Microstructure and mechanical properties of  $\text{Al}_x\text{CoCrFeNi}$  high-entropy alloys at elevated temperatures. *J Alloy Comp*. 2014;589:143. <https://doi.org/10.1016/j.jallcom.2013.11.084>.
- [36] Yang YTF, Xia SQ, Liu S, Wang CX, Liu SS, Zhang Y, Xue JM, Yan S, Wang YG. Effects of Al addition on microstructure and mechanical properties of  $\text{Al}_x\text{CoCrFeNi}$  high-entropy alloy. *Mater Sci Eng A*. 2015;648:15. <https://doi.org/10.1016/j.msea.2015.09.034>.
- [37] Niu C, Zaddach AJ, Oni AA, Sang X, Hurt JW III, LeBeau JM, Koch CC, Irving DL. Spin-driven ordering of Cr in the equiatomic high entropy alloy  $\text{NiFeCrCo}$ . *Appl Phys Lett*. 2015;106(16):299. <https://doi.org/10.1063/1.4918996>.
- [38] Ding Q, Zhang Y, Chen X, Fu X, Chen D, Chen S, Gu L, Wei F, Bei H, Gao Y. Tuning element distribution, structure and properties by composition in high-entropy alloys. *Nature*. 2019;574(7777):223. <https://doi.org/10.1038/s41586-019-1617-1>.
- [39] Tong Y, Zhao S, Bei H, Egami Y, Zhang YF. Severe local lattice distortion in Zr- and/or Hf-containing refractory multi-principal element alloys. *Acta Mater*. 2020;183:172. <https://doi.org/10.1016/j.actamat.2019.11.026>.
- [40] Chen XX, Wang Q, Cheng Z, Zhu M, Zhou H, Jiang P, Zhou L, Xue Q, Yuan F, Zhu J, Wu X. Direct observation of chemical short-range order in a medium-entropy alloy. *Nature*. 2021;592(7856):712. <https://doi.org/10.1038/s41586-021-03428-z>.
- [41] Xu XD, Liu P, Guo S, Hirata A, Fujita T, Nieh T, Liu CT, Chen MW. Nanoscale phase separation in a fcc-based  $\text{CoCrCuFeNiAl}_{0.5}$  high-entropy alloy. *Acta Mater*. 2015;84:145. <https://doi.org/10.1016/j.actamat.2014.10.033>.
- [42] Afa B, Gol C, Ammb D, Kasatikov S, Scherb S, Huthwelker T, Acapito F, Schumacher G. Short-range chemical order and local lattice distortion in a compositionally complex alloy - ScienceDirect. *Acta Mater*. 2020;193:329. <https://doi.org/10.1016/j.actamat.2020.04.034>.
- [43] Fernández-Caballero A, Wróbel JS, Mummery PM, Nguyen-Manh D. Short-range order in high entropy alloys: theoretical formulation and application to Mo-Nb-Ta-V-W system. *J Phase Equilib Diffus*. 2017;38(4):391. <https://doi.org/10.1007/s11669-017-0582-3>.
- [44] Körmann F, Ruban AV, Sluiter MHF. Long-ranged interactions in bcc  $\text{NbMoTaW}$  high-entropy alloys. *Mater Res Lett*. 2017;5(1):35. <https://doi.org/10.1080/21663831.2016.1198837>.
- [45] Pan Y, Pu DL, Yu ED. Structural, electronic, mechanical and thermodynamic properties of Cr-Si binary silicides from first-principles investigations. *Vacuum*. 2020;185:110024. <https://doi.org/10.1016/j.vacuum.2020.110024>.
- [46] Yurchenko N, Stepanov N, Salishchev G. Laves-phase formation criterion for high-entropy alloys. *Mater Sci Technol MST Publ Inst Metals*. 2017;704:82. <https://doi.org/10.1080/02670836.2016.1153277>.
- [47] Stepanov ND, Shaysultanov DG, Ozerov MS, Zhrebtsov SV, Salishchev GA. Second phase formation in the  $\text{CoCrFeNiMn}$  high entropy alloy after recrystallization annealing. *Mater Lett*. 2016;185:1. <https://doi.org/10.1016/j.matlet.2016.08.088>.
- [48] Stepanov ND, Yurchenko NY, Sokolovsky VS, Tikhonovsky MA, Salishchev GA. An  $\text{AlNbTiVZr}_{0.5}$  high-entropy alloy combining high specific strength and good ductility. *Mater Lett*. 2015;161:136. <https://doi.org/10.1016/j.matlet.2015.08.099>.
- [49] Pan Y, Guan WM. The hydrogenation mechanism of PtAl and IrAl thermal barrier coatings from first-principles investigations. *Int J Hydrogen Energy*. 2020;45(38):20032. <https://doi.org/10.1016/j.ijhydene.2020.04.290>.
- [50] Wang L, Chen SS, Li BL, Cao TQ, Wang BP, Wang L, Ren Y, Liang J, Xue YF. Lightweight  $\text{Zr}_{1.2}\text{V}_{0.8}\text{NbTiAl}$  high-entropy alloys with high tensile strength and ductility. *Mater Sci Eng, A*. 2021;814:141234. <https://doi.org/10.1016/j.msea.2021.141234>.
- [51] Zhang Y, Zuo TT, Tang Z, Gao MC, Dahmen KA, Liaw PK, Lu ZP. Microstructures and properties of high-entropy alloys. *Prog Mater Sci*. 2014;61:1. <https://doi.org/10.1016/j.pmatsci.2013.10.001>.
- [52] Liu WH, Lu ZP, He JY, Luan JH, Wang ZJ, Liu B, Li Y, Chen MW, Liu CT. Ductile  $\text{CoCrFeNiMo}_x$  high entropy alloys strengthened by hard intermetallic phases. *Acta Mater*. 2016;116:332. <https://doi.org/10.1016/j.actamat.2016.06.063>.
- [53] Ming K, Bi X, Wang J. Precipitation strengthening of ductile  $\text{Cr}_{1.5}\text{Fe}_{2.0}\text{Co}_{3.5}\text{Ni}_{2.0}\text{Mo}_{1.0}$  alloys. *Scripta Mater*. 2017;137:88. <https://doi.org/10.1016/j.scriptamat.2017.05.019>.
- [54] He JY, Wang H, Huang HL, Xu XD, Chen MW, Wu Y, Liu XJ, Nieh TG, An K, Lu ZP. A precipitation-hardened high-entropy alloy with outstanding tensile properties. *Acta Mater*. 2016;102:187. <https://doi.org/10.1016/j.actamat.2015.08.076>.
- [55] Gwalani B, Soni V, Lee M, Mantri SA, Ren Y, Banerjee R. Optimizing the coupled effects of Hall-Petch and precipitation strengthening in a  $\text{Al}_{0.3}\text{CoCrFeNi}$  high entropy alloy. *Mater Des*. 2017;121:254. <https://doi.org/10.1016/j.matdes.2017.02.072>.
- [56] Wang ZG, Zhou W, Fu LM, Wang JF, Luo RC, Han XC, Chen B, Wang XD. Effect of coherent L12 nanoprecipitates on the tensile behavior of a fcc-based high-entropy alloy. *Mater Sci Eng*. 2017;696:503. <https://doi.org/10.1016/j.msea.2017.04.111>.
- [57] Zhao YL, Yang TY, Tong Y, Wang T, Luan JH, Jiao ZB, Chen D, Yang YY, Hu A, Liu CT, Kai JJ. Heterogeneous precipitation behavior and stacking-fault-mediated deformation in a  $\text{CoCrNi}$ -based medium-entropy alloy. *Acta Mater*. 2017;138:72. <https://doi.org/10.1016/j.actamat.2017.07.029>.
- [58] Wani IS, Bhattacharjee T, Sheikh S, Bhattacharjee PP, Guo S, Tsuji N. Tailoring nanostructures and mechanical properties of  $\text{AlCoCrFeNi}_{2.1}$  eutectic high entropy alloy using thermo-mechanical processing. *Mater Sci Eng*. 2016;675:99. <https://doi.org/10.1016/j.msea.2016.08.048>.
- [59] Li Z, Pradeep KG, Deng Y, Raabe D, Tasan CC. Metastable high-entropy dual-phase alloys overcome the strength-ductility trade-off. *Nature*. 2016;534(7606):227. <https://doi.org/10.1038/nature17981>.
- [60] Lu Y, Gao X, Jiang L, Chen Z, Wang T, Jie J, Kang H, Zhang Y, Guo S, Ruan H, Zhao Y, Cao Z, Li T. Directly cast bulk eutectic and near-eutectic high entropy alloys with balanced strength and ductility in a wide temperature range. *Acta Mater*. 2017;124:143. <https://doi.org/10.1016/j.actamat.2016.11.016>.
- [61] Choi WM, Hee Y, Dong J, Kim G, Su S. A thermodynamic modelling of the stability of sigma phase in the Cr-Fe-Ni-V high-entropy alloy system. *J Phase Equilib Diffus*. 2018;39(5):694. <https://doi.org/10.1007/s11669-018-0672-x>.
- [62] Liang YJ, Wang LJ, Wen YR, Chen BY, Wu QL, Cao TQ, Xiao Q, Xue YF, Sha G, Wang Y, Ren Y, Li X, Wang L, Wang FC, Cai HN. High-content ductile coherent nanoprecipitates achieve ultrastrong high-entropy alloys. *Nat Commun*. 2018;8:1. <https://doi.org/10.1038/s41467-018-06600-8>.
- [63] Gwalani B, Soni V, Choudhuri D, Lee M, Hwang JY, Nam SJ, Banerjee R. Stability of ordered L1(2) and B-2 precipitates in face centered cubic based high entropy alloys- $\text{Al}_{0.3}\text{CoFeCrNi}$  and  $\text{Al}_{0.3}\text{CuFeCrNi}_2$ . *Scripta Mater*. 2016;123:130. <https://doi.org/10.1016/j.scriptamat.2016.06.019>.

